RMetS
Royal Meteorological Society

High gravity-wave activity observed in Patagonia, Southern America: generation by a cyclone passage over the Andes mountain range

M. Pulido,[ab]* C. Rodas,[a] D. Dechat[c] and M. M. Lucini[bc]

[a]*Department of Physics, FACENA, Universidad Nacional del Nordeste, Corrientes, Argentina*
[b]*CONICET, Argentina*
[c]*Department of Mathematics, FACENA, Universidad Nacional del Nordeste, Corrientes, Argentina*

*Correspondence to: M. Pulido, Department of Physics, FACENA, Universidad Nacional del Nordeste, Av. Libertad 5400, 3400 Corrientes, Argentina. E-mail: pulido@unne.edu.ar

The Antarctic peninsula and Patagonia region (the south of South America) have recently been identified as the regions with the highest gravity-wave activity in the world. In this work, the generation and propagation of gravity waves in the Patagonia region in an event of strong wave activity from 30 October 1995–1 November 1995 is examined by means of radiosonde measurements and simulations with the Weather Research and Forecasting (WRF) model. The waves are generated by strong surface winds found near the Andes mountains at a latitude of 49–51°S. The strong low-level winds are related to an extratropical cyclone that propagates southeastward in the South Pacific ocean and approaches the western coast of the continent. The waves propagate southeast toward Tierra del Fuego and they continue their propagation over the Drake Passage. They are found to propagate long meridional (lateral) distances due to the shear background conditions. This fact is corroborated with WRF simulations and a novel technique that combines wavelet analysis and backward ray-tracing. Therefore, this work provides further evidence that high gravity-wave activity found by several studies over Drake Passage may have an orographic origin. During the orographic wave event, which lasts about 72 hours, the horizontal wavelength is unexpectedly found to change day-to-day. The analysis shows that changes in the near-surface meteorological conditions produced by the cyclone passage may trigger different components of the forcing orography. The orographic waves propagate toward their critical levels, which are found at 25 km and above. The radiosonde measurements show that the wave is breaking continuously along a wide altitude range; this finding from measurements supports the picture of continuous wave erosion along the ray path instead of abrupt wave-breaking for the examined wave event. **Copyright © 2012 Royal Meteorological Society**

Key Words: orographic waves; wave breaking; ray-tracing

Received 7 October 2011; Revised 2 March 2012; Accepted 25 April 2012; Published online in Wiley Online Library

Citation: Pulido M, Rodas C, Dechat D, Lucini MM. 2012. High gravity-wave activity observed in Patagonia, Southern America: generation by a cyclone passage over the Andes mountain range. *Q. J. R. Meteorol. Soc.* DOI:10.1002/qj.1983

1. Introduction

Recent observational studies based on satellite observations suggest that gravity-wave activity over South America and Antarctica is amongst the highest on the Earth (Eckermann and Preusse, 1999; Ern *et al.*, 2004; Wu and Eckermann, 2008; Alexander *et al.*, 2008; Alexander *et al.*, 2009; Alexander *et al.*, 2010). Wu and Eckermann

Copyright © 2012 Royal Meteorological Society

(2008), examining satellite observations, found an important maximum of global gravity-wave activity in the region over Patagonia and the Antarctic peninsula during July 2005. Thus, the region is a natural laboratory in which to investigate gravity-wave properties.

Pulido and Thuburn (2008) examine the effects of gravity waves on the general circulation using an inverse technique based on variational data-assimilation principles. In a global analysis, they show that strong momentum fluxes are found over the Himalayas and Antarctica and in a localized region over the southern part of the Andes mountain range. The magnitude of momentum fluxes found over Antarctica and Patagonia reaches values of 0.1 hPa; these maximum values are found between September and November 2002.

There are also some works that focus on large wave amplitude case studies over the Patagonia region and Antarctica. Eckermann and Preusse (1999) found a large-amplitude wave event with wave-breaking amplitudes over Patagonia with Cryogenic Infrared Spectrometer Telescope for Atmosphere (CRISTA) measurements. Alexander and Teitelbaum (2007) examined a large wave-amplitude event which occurred at the Antarctic peninsula and was captured by the Atmospheric Infrared Sounder (AIRS) instrument. This event was also present in European Centre for Medium-Range Weather Forecasts (ECMWF) analysis; the authors showed that strong surface winds are crossing the Antarctic peninsula mountains and the waves found in the ECMWF analysis are stationary, so that they concluded that the observed perturbations are mountain waves. Plougonven *et al.* (2008) examined one of the balloons belonging to the VORCORE campaign, which exploded over the Antarctic peninsula; they found that a large-amplitude orographic gravity wave occurred over the peninsula, reaching peak-to-peak variations in the zonal wind of 25–30 m s^{-1} (zonal wind amplitudes of about 12.5–15 m s^{-1}) at the moment that the balloon exploded.

In principle the main source of the gravity waves observed over South America and Antarctica is not clear. The orographic forcing, convection and spontaneous geostrophic adjustment are probable generation mechanisms in the south of South America. A deeper tropospheric jet stream is found in the Southern Hemisphere due to the reduced surface friction; the longitudinally and seasonally averaged zonal wind has a peak at 50°S and 850 hPa of 10–20 m s^{-1} (e.g. Holton, 1992, p. 143); gusts may increase these values by at least a factor of 4. Strong surface winds are usually present in Patagonia, a place particularly suitable for wind electricity generation. When perturbations over the tropospheric jet stream reach the South American continent, they find the Andes mountain range, so gravity-wave generation by orography is highly probable on the lee side of the Andes between 35°S and 55°S.

The maximum time-averaged zonal winds are regions where synoptic waves tend to develop and propagate downstream along the storm tracks. The zonal wind jet coincides roughly with the region where the South Pacific storm tracks are located (Trenberth, 1991). The development of baroclinic waves is an important source of inertia–gravity waves (O'Sullivan and Dunkerton, 1995). The baroclinic wave development produces a distortion in the tropospheric jet stream; the flow is then adjusted toward geostrophic balance from the imbalance state, triggering inertia–gravity waves. This occurs mainly in the exit region of the jet stream where the imbalance is more marked, as has been found in observations (Uccellini and Koch, 1987). Convective activity is usually associated with the baroclinic development along the jet stream, so that gravity waves generated by convective processes (Vincent *et al.*, 2004) are expected in the region as well. Gravity waves induced by convective processes have been observed in extratropical regions by Chun *et al.* (2007) using radiosonde measurements. Strong gravity-wave activity has been found near the jet in simulations with a general circulation model that includes a convective gravity-wave parametrization (Song et al, 2007).

The breaking of large-amplitude gravity waves may play a major role in the dynamics of the middle atmosphere of the Southern Hemisphere. In this hemisphere the planetary-wave activity is weaker than in the Northern Hemisphere; this is believed to be due mainly to the lack of land–sea contrast in the Southern Hemisphere. Garcia and Boville (1994) noted that gravity-wave drag compensates for the lack of planetary-wave drag, producing important dynamical effects as low as 20 km by means of the downward control principle. As a result of this weak planetary-wave activity, the nocturnal jet found in the middle atmosphere of the Southern Hemisphere is stronger than the one in the Northern Hemisphere. In this environment with strong background winds, gravity waves with small intrinsic phase speed may propagate higher in the middle atmosphere, including waves from orographic sources. This will produce a stronger gravity-wave drag. Pulido and Thuburn (2008) corroborate this; they found that the winter deceleration centre in the Southern Hemisphere, with a peak of 45 m s^{-1} day^{-1}, is stronger by about a factor of 1.5 compared with the Northern Hemisphere deceleration centre.

In this work we present a detailed case study from radiosonde observations launched at Ushuaia, Tierra del Fuego (Argentina) in an attempt to characterize the frequent high-amplitude waves observed over high latitudes of the Southern Hemisphere in the winter–spring season. Because of the unique characteristics of the region in investigating gravity waves, there is a major field experiment planned for the region in 2013 called the Southern Andes ANtarctic GRavity wave InitiAtive (SAANGRIA). So far, the radiosonde measurements at Ushuaia that we examined in this work comprise one of the few campaigns that have been performed in this region. The location where the radiosondes were launched is ideal to study the sources of high-amplitude waves. Measurements from radiosondes produce a very high vertical resolution profile with information regarding temperature and velocity from the ground up to 30–35 km, so that they give complementary information to that found in the region by satellite observations. Indeed this high vertical resolution allows us to investigate the breaking properties of the waves, a process that it is not possible to examine with satellite observations. The spectral ranges captured by different measurement instruments are detailed in Alexander *et al.* (2010). Furthermore, the use of Weather Research and Forecasting (WRF) simulations during the wave event with ECMWF analysis data as initial and boundary conditions helps to determine the subtle gravity-wave source mechanism. One intriguing aspect is that high wave activity is also found over the seas, suggesting that gravity-wave sources may be non-orographic. Propagation of orographic waves may also give an explanation for the gravity-wave activity found over the seas around the

Copyright © 2012 Royal Meteorological Society

south of South America and the Antarctic peninsula. Long propagation of orographic waves has been observed in the region using AIRS data (Alexander and Teitelbaum, 2007).

The radiosonde measurements are presented and analyzed in section 2. The WRF model simulations are described and examined in section 3. We focus on the source generation mechanism, particularly on the synoptic situation that might give favourable conditions to trigger this high wave activity event (section 3.1). The propagation of the waves is investigated using backward ray-tracing; we show that lateral shear of the background flow deflects the wave trajectories (section 3.3). We use a novel approach that combines horizontal wavelet analysis and ray-tracing to follow waves from the observed heights to the sources. This approach gives conclusive results on the location of the mountains that act as sources of the wave event. The role of gravity-wave filtering is addressed in section 3.4. Finally, conclusions are given in section 4.

2. Radiosonde observations

A few short radiosonde campaigns have been performed in Patagonia. In this work we examine one of these radiosonde campaigns, motivated by the several satellite observations that found high wave activity in this region. The campaign was conducted by the Centre National d'Etudes Spatiales (CNES, France) from 25 October 1995–20 December 1995; within this period 25 radiosondes were launched from Ushuaia (Argentina) located at 54.7°S, 68.1°W.* After a preliminary study of the wave activity observed in all the radiosondes, we decided to focus on a very high wave activity event that was captured by two radiosondes launched on 30 October 1995 and 1 November 1995.

The height range covered by the radiosondes goes from ground to about 30–35 km. Measurements were made with a time step of 10 s, which implies a vertical resolution of about 50 m. The points are then equispaced in height using a cubic spline technique with a vertical resolution of 40 m. If an outlier point is detected, it is rejected and its value is replaced by a cubic interpolation between neighbour points.

Figure 1 shows the zonal and meridional wind measured by the radiosonde launched on 30 October. There is a strong southward wind that peaks at 12 km; a strong shear region is located aloft where gravity-wave activity enhances. These traces of wave activity are visible in the total wind profiles (Figure 1). On 1 November the vertical profiles of zonal and meridional wind, shown in Figure 2, present stronger perturbations with peak-to-peak variations reaching 20–25 m s^{-1}. The background wind is obtained by a low-pass filter of 10 km vertical wavelength. The zonal background wind reaches 50 m s^{-1} at 12 km and diminishes aloft: at 35 km the zonal background wind is zero. The intensity of the meridional background wind is also maximum at 12 km where it reaches 35 m s^{-1}. The meridional background wind is zero at 25 km. Regrettably the radiosonde on 1 November has a gap in wind measurements around 10 km. The missing data were

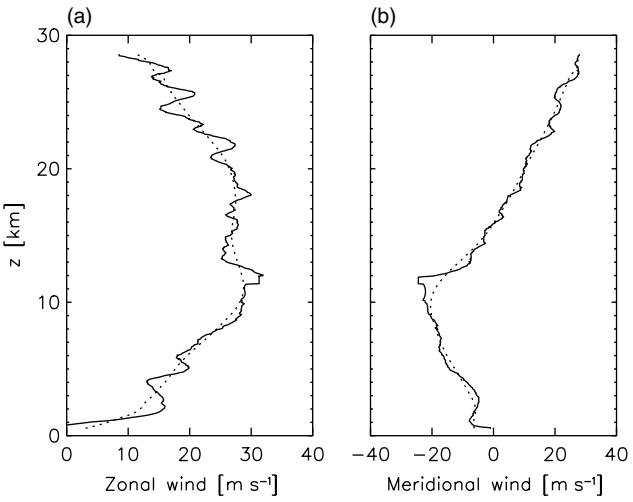

Figure 1. Zonal (a) and meridional (b) wind profiles measured by the radiosonde launched on 30 October. The background wind profile given by a low-pass filter of 10 km is also shown (dotted line). The radiosonde was launched at 1154 UTC.

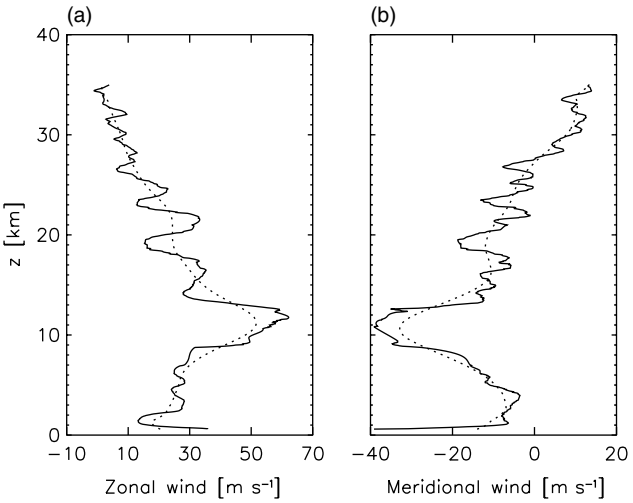

Figure 2. As Figure 1 but on 1 November. The radiosonde was launched at 1144 UTC.

filled with a cubic fit. Cubic fitting the data across this short missing height region did not influence the wave characteristics.

In order to examine the perturbations in the velocity and temperature radiosonde profiles, we applied a band filter (Scavuzzo *et al.*, 1998) with a filtering window of 1–10 km. This wide window keeps all the information of the perturbations, including the main vertical wavelength of the disturbance, which from direct inspection is about 5 km (also confirmed by a wavelet analysis). Furthermore, this window does not filter the refraction toward the higher vertical wavenumber that the wave field is suffering as the horizontal background wind diminishes with height. The wind perturbations, in Figure 3, present the highest wave activity just above the tropopause (at 9 km) in both radiosondes on 30 October and 1 November.† Regarding the

*This campaign was not focused on gravity-wave activity but on the dynamics of the Antarctic vortex edge during its breaking; it was a preliminary experiment before constant-pressure balloon campaigns. Regrettably, because of this the launch of the radiosondes is not daily but sporadic, which did not allow us a statistical analysis of gravity-wave activity.

†One should be cautious with the maximum wave amplitudes found at the jet height, since these perturbations could be an artefact of the filtering technique, which may not work properly in the presence of the jet assigning part of it to the wave field.

Copyright © 2012 Royal Meteorological Society

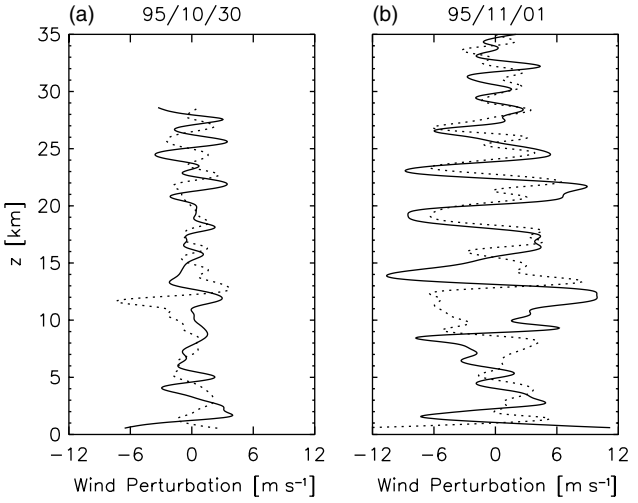

Figure 3. Zonal (continuous line) and meridional (dotted line) wind perturbations obtained with a filtering window of 1–10 km on (a) 30 October and (b) 1 November.

temporal evolution, from the WRF simulations (section 3) we deduce that the disturbance starts to develop on 30 October and persists until 1 November so that the radiosondes correspond to the same forcing event. For the 30 October radiosonde, the vertical wavelength of the perturbations is not clear (Figure 3(a)); a superposition of waves appears to be present. For the 1 November radiosonde, the meridional and zonal wind components are in phase in the troposphere and the vertical wavelength is about 8 km (Figure 3(b)). In the stratosphere the perturbation field exhibits different characteristics from those in the troposphere and the vertical wavelength is much shorter, 4–5 km. Since the vertical wavelength is inversely proportional to the Brunt–Väisälä frequency, the vertical wavelength change is consistent with a Brunt–Väisälä frequency increase of a factor of 2 in the stratosphere. The wind perturbation components in the stratosphere are not in phase, suggesting, in principle, the presence of inertia–gravity waves with intrinsic periods that are a significant fraction of the inertial period. The amplitude of the perturbations diminishes above 27 km and the vertical wavelength is shortening as the wave propagates toward that height. A critical layer may be developing above 27 km.

Figure 4 shows the hodographs for the wind perturbations as a function of height. The wind profile is filtered with a 1–10 km window to obtain the perturbations. The superposition of different waves may produce the noise found in the hodograph; narrower filter windows show a clearer elliptical polarization. The hodograph allows the horizontal propagation direction to be inferred. The ratio between the intrinsic and inertial frequencies may also be inferred from the hodograph. The rotation of the wind vector is counter-clockwise in both hodographs, indicating that wave energy propagates upward as expected. Surprisingly the hodograph for 30 October shows a rather circular polarization; this would indicate an intrinsic frequency close to the inertial frequency. Because of the circular polarization found and the presence of noise, the direction of propagation cannot be determined. In the case of the 1 November hodograph, an elliptical polarization is found in the 22–26 km height range; the angle of the major axis is about 34 ± 3 degrees and so is the horizontal wavenumber direction. The azimuthal angle of wave energy propagation, which is expected to be perpendicular to the horizontal wavenumber vector, is therefore $-56 \pm 3^\circ$ (southeast direction). The ratio between the axes of the ellipse in the 1 November hodograph is 3.2 ± 0.3. This would indicate an intrinsic frequency of $3.2f$. The wind shear perpendicular to the direction of the horizontal wavenumber vector also induces a perturbation in that direction resulting in an elliptical polarization (Hines, 1989). This correction resulted negligible (within the error). From a wavelet analysis, the dominant vertical wavelength 22–26 km height range is 3.6 ± 0.1 km, so that from the hydrostatic dispersion relationship the dominant horizontal wavenumber can be inferred from

$$k_{\mathrm{H}} = \frac{m\sqrt{\hat{\omega}^2 - f^2}}{N_0} = (3.1 \pm 0.4) \times 10^{-5}\mathrm{m}^{-1}, \qquad (1)$$

where $\hat{\omega}$ is the intrinsic frequency and N_0 is the background Brunt–Väisälä frequency. Thus, the zonal and meridional wavelengths are $\lambda_x = (240 \pm 40)$ km and $\lambda_y = (370 \pm 60)$ km respectively. Finally, the ground-based frequency is given by $\omega = \hat{\omega} + \mathbf{k}_{\mathrm{H}} \cdot \mathbf{u}_{0\mathrm{H}}$. The estimated Doppler shifting term is $\mathbf{k}_{\mathrm{H}} \cdot \mathbf{u}_{0\mathrm{H}} = (3.8 \pm 0.4) \times 10^{-4}\,\mathrm{s}^{-1}$ so that the ground-based frequency is zero within the measurement errors. Therefore, the waves are stationary; this indicates the possible existence of mountain waves.

Figure 5 shows the Richardson number for both radiosondes. The wind and temperature fields were filtered with a 1 km low-pass filter to eliminate artificial small Richardson values produced by noise and to focus only on the wave event. On 30 October, the *Ri* profile shows that the flow is stable dynamically with a *Ri* greater than 1, except at the lowest heights where a burst in the wind produces a patch of small Richardson number. On 1 November, the wave field is clearly destabilizing the flow in several patches; these patches present dynamical instabilities, suggesting that the wave field is saturated and probably breaking. The unstable patches are found in the troposphere and in the stratosphere up to 26 km. This *Ri* profile indicates that the wave is saturated along its whole path. The amplitude of the wave is controlled by the processes (i.e. turbulence) related to the dynamical instability that the waves produce in those patches. However, the wave still continues its upward propagation. Convective instabilities are not found in the stratosphere (the Brunt–Väisälä frequency is shown with dashed lines in Figure 5(b)). Figure 5(c)) shows the background *Ri*; large values are found in the stratosphere so that the wave is the main thing responsible for producing the instability.

3. Mesoscale model simulations

We complement the analysis of the radiosondes with high-resolution numerical simulations using the WRF model (Skamarock *et al.*, 2005) version 3.1. The simulations were produced using ERA-interim reanalysis data (Simmons *et al.*, 2007) as initial and boundary conditions. The domain we use is shown in Figure 6; it covers a region of 3000 km × 2400 km around Ushuaia. The initial conditions are taken on 30 ctober 1995 at 0000 UTC and the WRF model is run for 84 hours up to 2 November 1995 at 1200 UTC with a time step of 60 s.

There are 65 vertical levels, covering from the surface up to 10 hPa, with a vertical resolution of about 500 m.

Copyright © 2012 Royal Meteorological Society

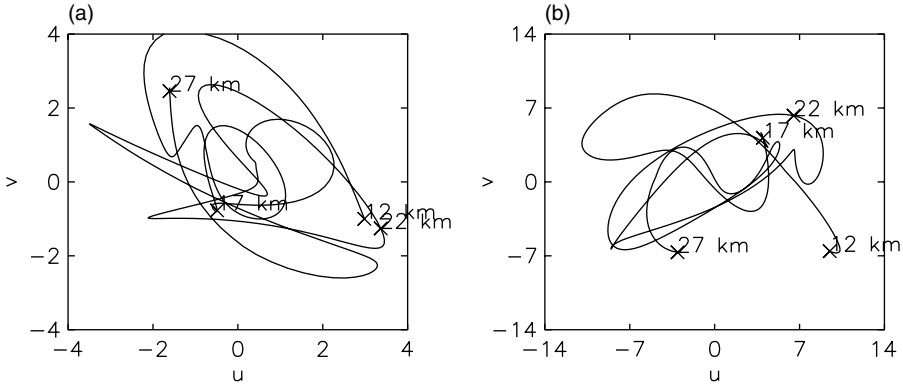

Figure 4. Hodograph for the wind perturbation obtained with a 1–10 km filtering window from the radiosondes on (a) 30 October and on (b) 1 November.

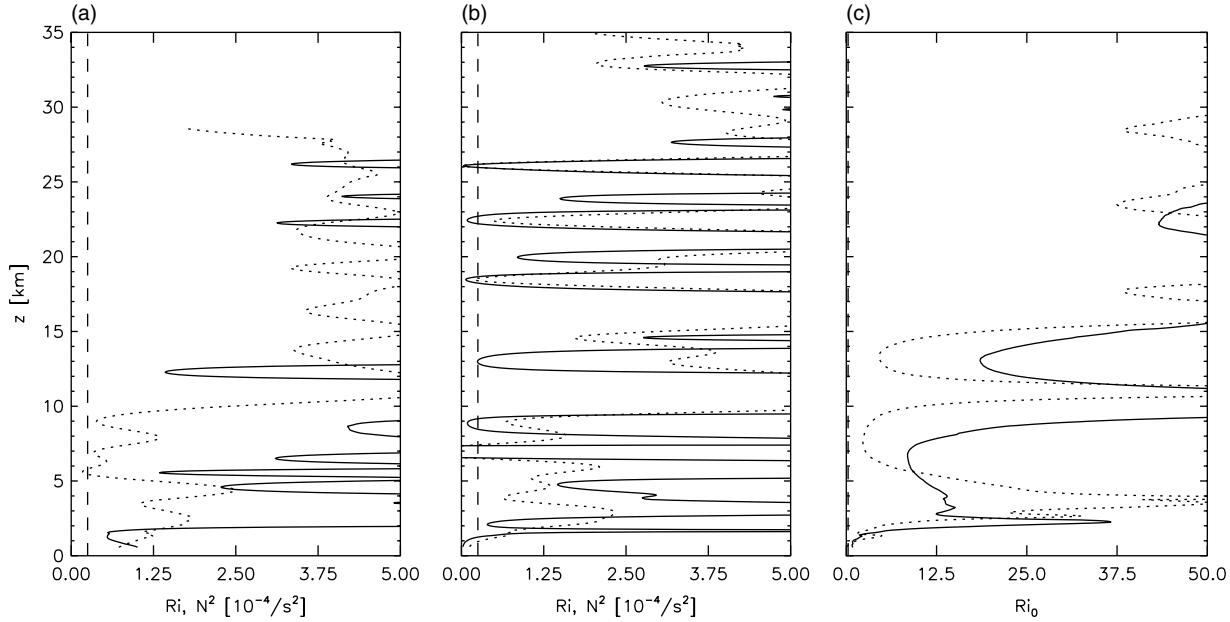

Figure 5. Richardson number (continuous line) and the square of the Brunt–Väisälä frequency (dotted line, $[N^2] = 1.e-4\,\mathrm{s}^{-2}$) from the radiosondes on (a) 30 October and (b) 1 November. The temperature and wind profiles are filtered with a 1 km wavelength. (c) The background *Ri* for 30 October (continuous line) and 1 November (dotted line). Vertical lines (dashed lines) show $Ri = 0.25$.

The horizontal resolution is 30 km. Preliminary simulations (including a 10 km horizontal resolution simulation) showed that a 30 km horizontal resolution was enough to represent the observed waves. The vertical resolution that we use is 500 m in order to represent critical layer processes as precisely as possible. A sponge layer of 8 km depth at the top of the WRF model is set using Rayleigh friction with a coefficient of $0.1\,\mathrm{s}^{-1}$, which damps the waves and avoids spurious reflection of waves at the top. The convective scheme is turned off for the control simulations.

3.1. *Generation of the disturbance*

In this section we focus on the generation mechanism of the wave event. If its origin is related to the orography (see Figure 6) then two groups of mountains may force the perturbations that are captured by the radiosondes. One is the mountain located on Tierra del Fuego island just westward of the launch site with a height of 800 m. The other mountains that may contribute to the observed perturbation are the continental mountains located at about 49.3°S, the maximum height of which reaches 1740 m (in the WRF orography). Thus, the wave generation mechanism is further examined from WRF simulations.

The synoptic situation that coincides with the generation of the disturbance corresponds to an important extratropical cyclone that is located in the South Pacific ocean. We use an objective technique to detect and track the cyclone trajectory (Blender *et al.*, 1997) using the geopotential at 1000 hPa from ERA interim reanalysis data. The details on the cyclone-tracking technique are given in Appendix A. The extratropical cyclone genesis is found on 28 October at 0000 UTC and then it propagates southeastward (see Figure 7). On 30 October at 0000 UTC, the cyclone reaches the South American west coast. At this time, a discontinuous change in the direction of the cyclone trajectory is found (the temporal resolution of the cyclone-tracking technique is that of the ERA interim reanalysis, six hours). This direction change is related to the cyclone pattern, which is elongated in the east–west direction on 30 October at 0000 UTC (Figure 7(a)). As the cyclone starts interacting with the mountain range, its major axis changes to a northwest–southeast direction (Figure 7(b)). On 31 October at 0000 UTC, the cyclone is located to the south of Tierra del

Copyright © 2012 Royal Meteorological Society

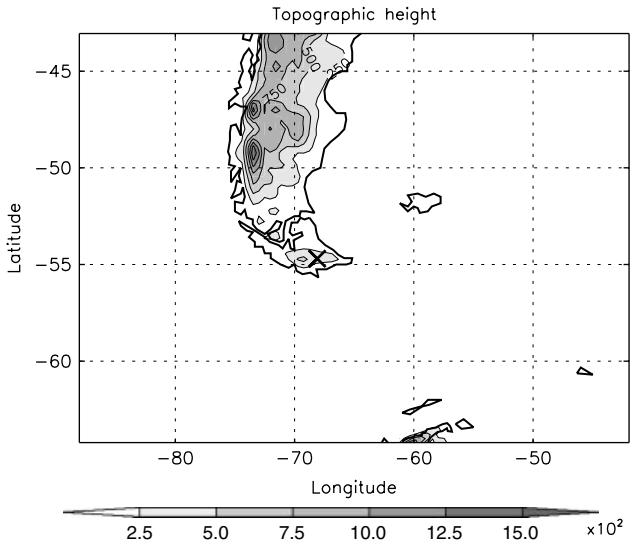

Figure 6. Model domain (the model domain coincides with the region shown in the plot) and orography (m) used in the WRF simulations. The location of Ushuaia, where the radiosondes were launched, is shown with a cross.

Fuego and a strong flow is expected to cross the continent (Figure 7(c)). On 1 November at 0000 UTC, the cyclone is located near the Antarctica peninsula and the strong surface flow crossing the Andes mountain range remains. At later times the cyclone weakens and so does the flow crossing the Andes.

The cyclone life cycle is rather well represented in the WRF simulation; Figure 8 shows the wind vector at the second model sigma level. The cyclonic movement and its evolution from the surface wind in the WRF simulation (Figure 8) clearly coincide with the geostrophic wind resulting from the ERA interim data shown in Figure 7. Mountain waves are expected to be generated by the strong surface winds produced by the extratropical cyclone. The mountain forcing starts on 30 October at 0000 UTC (Figure 8(a)). At 1200 UTC the flow is crossing the Andes mountain range, particularly at the continental mountains (Figure 8(b)). The surface forcing is found to maximize its strength on 31 October at 0000 UTC (Figure 8(c)). The surface wind direction changes during the evolution as the cyclone moves southward, so that the generated wave field must change its characteristics during this period. The magnitude of the surface wind also has a diurnal oscillation corresponding to the cyclone evolution; therefore the generated wave field is also expected to be modulated by non-stationary waves.

Figure 9 shows the zonal wind component of the wave disturbance at 16 km simulated by WRF. The background wind has been removed by an averaging moving window (the window uses 40 points, i.e. 1200 km, in the zonal and meridional directions). Waves with a large amplitude, about 7 m/s in the zonal wind component, start penetrating the stratosphere on 30 October at 1200 UTC. The wavenumber vector is mainly directed in the zonal direction; the horizontal wavelength is about 160 km on 30 October at 1200 UTC (Figure 9(a)), while 24 hours later the disturbance is extended toward the east and the horizontal wavelength is longer at this time, being 600 km. On 1 November, the disturbance is even stronger and is propagating toward the southeast, reaching 60°S with a dominant horizontal wavelength of about 270 km. Part of the disturbance is located above the Drake passage well away from the forcing location.

The day-to-day changes found in the horizontal wavelength during the same forcing event are unexpected. Three possible reasons for these changes are raised: (1) waves are forced by different mountains on different days, (2) changes in the background winds may refract horizontal wavelength, and (3) changes in stability conditions and in the surface winds (both in the direction and magnitude) may trigger a different spectrum of waves for realistic non-symmetric topography.

The wave characteristics found in Figure 9 appear to be correlated with the surface winds shown in Figure 8. Note that on 31 October the wavefront is parallel to the Andes mountain range (north–south) and a long zonal wavelength is found; this is related to the eastward wind found at the surface. On 1 November, the wavefronts of the disturbance are in the northwest–southeast direction; clearly this disturbance is related to the northeasterly surface winds that are seen in Figure 8(c). Therefore, the changes in horizontal wavelength could be related to changes in the direction of surface winds (produced by the propagation of the cyclone). The complex structure of the Andes around 50°S can be considered as a first approximation as an elongated obstacle with a border (see Figure 6). The cross-stream length of the mountain changes depending on the flow direction and thus a different spectrum of waves is excited. This would explain the changes in horizontal wavelength at 16 km. The temporal changes in the refraction due to changes in the background winds are examined in section 3.3. Time dependence of the horizontal background wind at the surface (Chen *et al.*, 2005) and in the lower layers may also contribute to these horizontal wavelength changes.

At 24 km of height, the wave pattern still shows a large amplitude with a peak-to-peak variation of 15 m s^{-1} (Figure 10). It propagates a very long distance downstream and laterally from the mountain, and is mainly located over the sea on 31 October and 1 November. Two factors may contribute to this long lateral propagation (by lateral we mean perpendicular to the downstream direction). One is the refraction by lateral shear; the impact of lateral shear for this long lateral propagation is evaluated in section 3.3. The other factor may be associated with one of the branches of the typical downstream ship-wave pattern (Smith, 1980) produced by an isolated mountain. The absence of waves over the highest mountains at latitudes equatorward of 52° is due to critical-level filtering. This produces the asymmetric pattern; the northern branch of the V-shaped pattern is completely obliterated by critical-level filtering. The variations in wind direction with height may also produce some impact on the observed wave pattern (Shutts, 1998).

Figure 11 shows the x–z cross-section of the vertical velocity at 49.3°S, which is the latitude of the highest mountain in the domain. The wave event is confined to altitudes lower than 20 km due to the presence of a critical layer at that height. On 30 October and 1 November, only the highest mountains are forcing the wave event. On the other hand, on 31 October the waves are not only forced by the mountain peak but also for the large Patagonian plateau; above it long waves are clearly visible. These long waves have a long horizontal propagation compared with the 'peak' waves, which propagate almost vertically in this x–z cross-section. This fact shows that, depending on the surface wind conditions, two kind of waves can be triggered by the

Copyright © 2012 Royal Meteorological Society

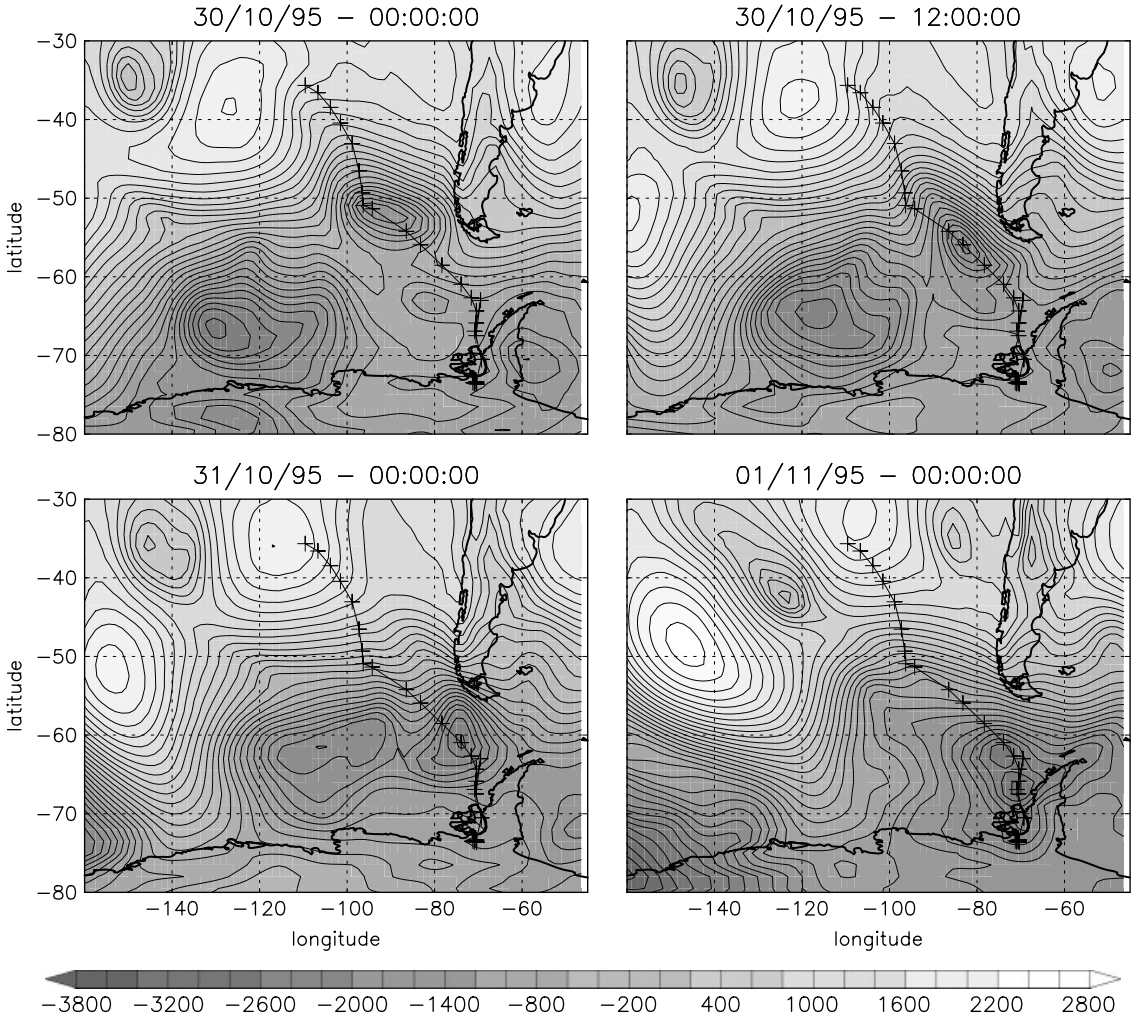

Figure 7. Geopotential (J kg^{-1}) at 1000 hPa from ERA interim reanalysis on (a) 30 October at 0000 UTC , (b) 30 October at 1200 UTC, (c) 31 October at 0000 UTC and (d) 1 November at 0000 UTC. Contour levels are each 200 J kg^{-1}. The cyclone trajectory is also shown. Crosses show the location of the cyclone eye at each reanalysis time. Crosses are shown starting from the first cyclone seed that is detected by the cyclone-tracking technique on 28 October at 0000 UTC. ERA interim reanalyses are every 6 h.

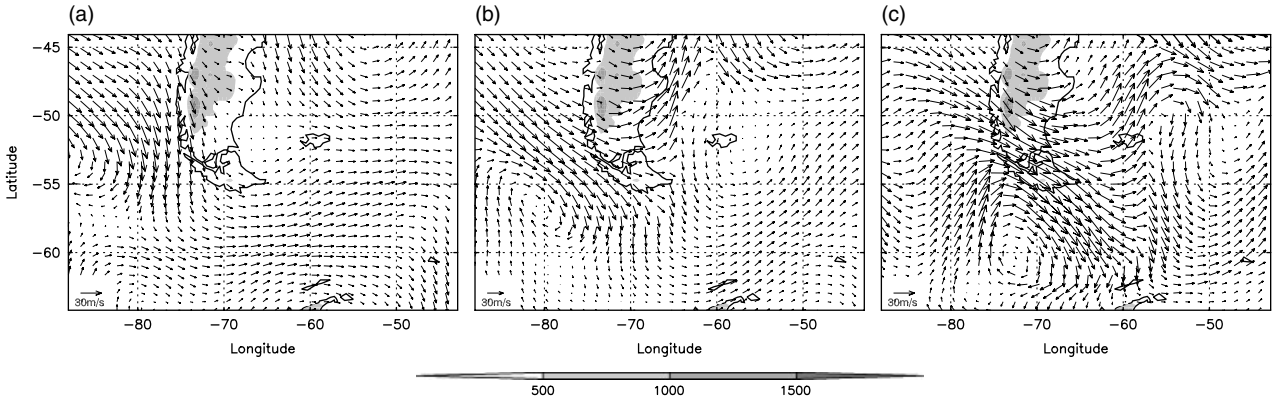

Figure 8. Wind vector at the second model sigma layer of the WRF simulation ($\approx$ 950 hPa over the sea) on (a) 30 October at 0000 UTC, (b) 30 October at 1200 UTC and (c) 31 October at 0000 UTC. (Only a fraction of grid points are plotted for a clearer representation.)

southern tip of the South American continent: short waves due to the Andes mountain range and a long-wavelength component forced by the plateau, which is about 400 km wide and 600 m of height. These long waves are found at 16 km in Figure 9. Short waves show three-dimensional characteristics; they present the V-shaped downstream ship-wave pattern of an isolated obstacle. On the other hand, the long waves appear to have two-dimensional characteristics; several parallel wave fronts are visible behind the two-dimensional ridge.

To evaluate whether all the wave energy found is due to mountain waves or another mechanism is at least partially involved in the generation of the waves, a simulation was conducted in which we set a flat South American continent with no topography (not shown). To perform this simulation we assigned to the velocity fields at each sigma level the

Copyright © 2012 Royal Meteorological Society

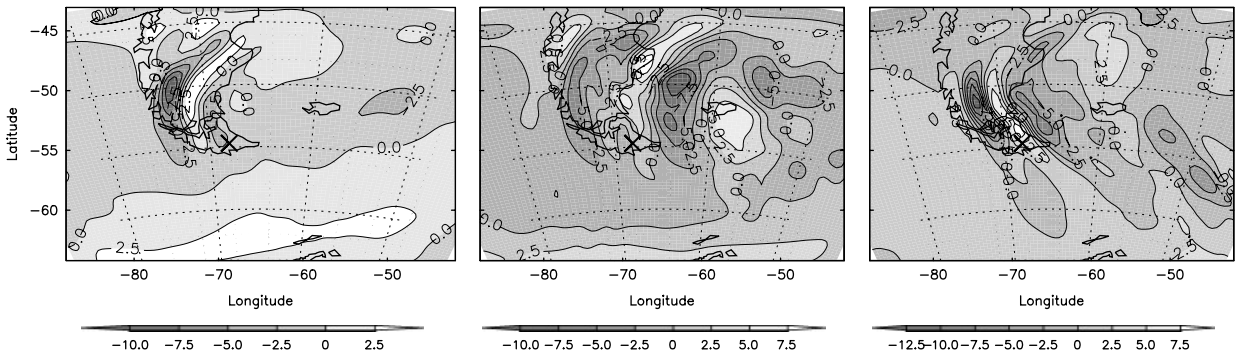

Figure 9. Zonal wind perturbation from the WRF simulation at 16 km on (a) 30 October at 1200 UTC, (b) 31 October at 1200 UTC and (c) 1 November at 1200 UTC. The location of Ushuaia is shown with a cross.

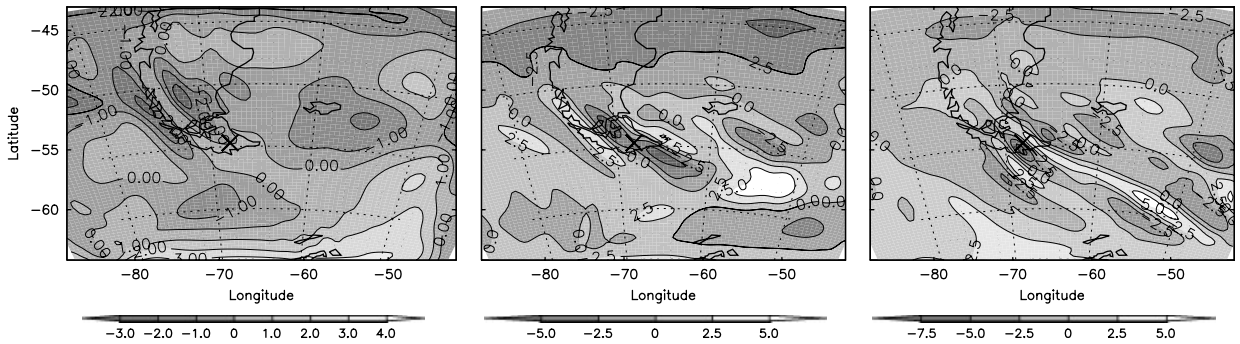

Figure 10. Zonal wind perturbation from the WRF simulation at 24 km on (a) 30 October at 1200 UTC, (b) 31 October at 1200 UTC and (c) 1 November at 1200 UTC.

corresponding initial field of the control simulation (case with topography). There were no signs of disturbance in this simulation; wave energy was practically negligible compared to the control simulation. Furthermore we also conducted a WRF simulation started on 25 October at 0000 UTC to investigate the influence of spin-up processes in the wave characteristics. The wave characteristics, including wave amplitude and wavelength, are essentially the same as those shown in Figures 9 and 10. Since there were signs of clouds in satellite images related to the low-pressure system, we also conducted a simulation with the representation of moist processes through the Lin scheme; the kinetic wave energy differences between the dry and moist simulations were small (about 10%). In this sense, our philosophy was to show the simulation capturing the main characteristics of the wave event that required the lowest computational resources.

3.2. *Propagation: vertical profiles and hodographs*

The zonal wind perturbation profiles obtained with a 1–10 km filtering window at a fixed horizontal position over Ushuaia and on 30 October at 1200 UTC and 1 November at 1200 UTC (close to the time that the radiosondes were launched, 1154 and 1144 UTC respectively) resulting from the WRF simulation and from the radiosondes are shown in Figure 12. On 30 October there is no agreement between the profiles; the 10 km horizontal resolution WRF simulation does not diminish the mismatch. The WRF simulation can only capture a long-wavelength component but not the short waves that are found in the radiosonde. On the other hand, on 1 November an excellent agreement is found for the WRF simulation of 30 km horizontal resolution in the 15–25 km height range: both the amplitude and phase of the disturbance simulated by the WRF are close to the radiosonde profile. Surprisingly, the WRF

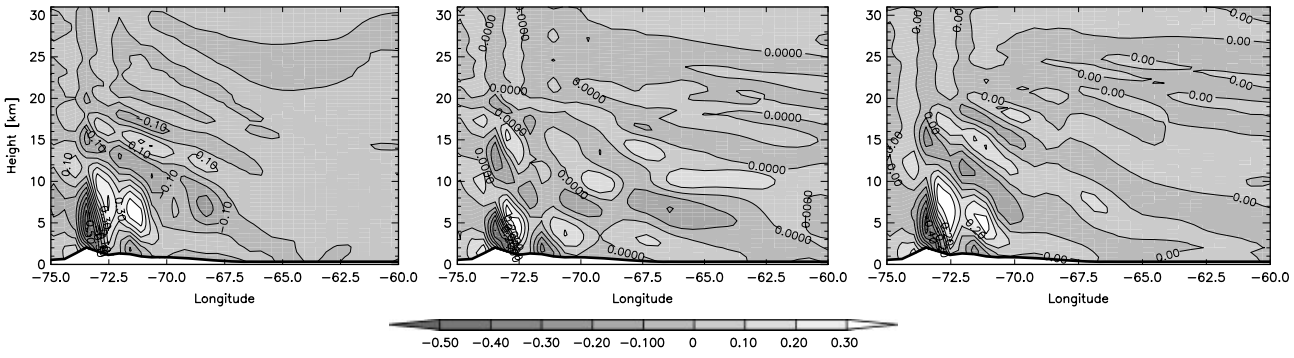

Figure 11. *x–z* cross-section of the vertical velocity at 49.3°S resulting from the WRF simulations on (a) 30 October at 1200 UTC, (b) 31 October 1200 UTC and (c) 1 November at 1200 UTC. The height of the orography is shown with a wide continuous line.

Copyright © 2012 Royal Meteorological Society

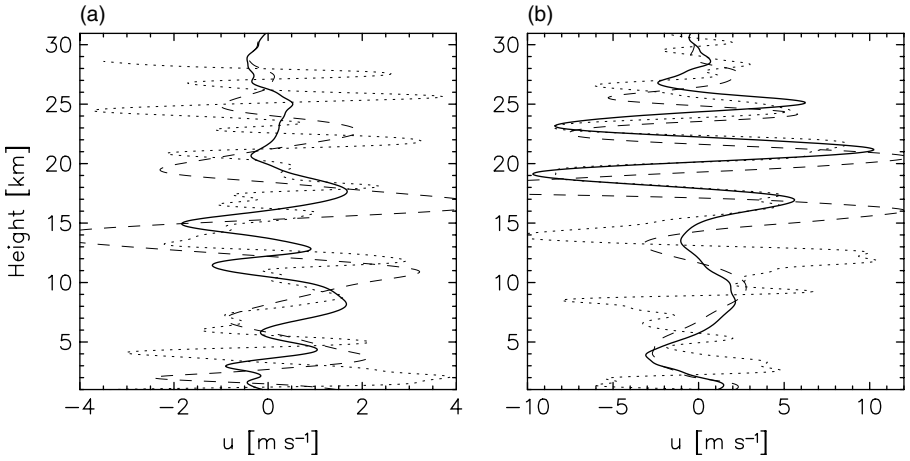

Figure 12. Zonal wind perturbation from the WRF simulations with a 30 km horizontal resolution (continuous line), 10 km horizontal resolution (dashed line) and radiosondes (dotted line) above Ushuaia on (a) 30 October at 1200 UTC and (b) 1 November at 1200 UTC. Perturbations are obtained with a filtering window of 1–10 km.

simulation of 10 km horizontal resolution deteriorates the agreement found for the 30 km simulation; both the phase and amplitude are degraded.

Figure 13 shows the hodographs from the wind perturbation vertical profiles (at a fixed time and horizontal position) over Ushuaia calculated from WRF simulations. Wind perturbations are obtained from WRF simulations with a filtering window of 1–10 km using the same procedure as the one used to obtain the hodographs from the radiosonde measurements (Figure 4).

In agreement with the radiosonde measurements, the wavefield given by the WRF simulation shows a clear elliptical polarization over Ushuaia. The sense of rotation of the horizontal wind vector as a function of height is mainly counter-clockwise in the three hodographs (see Figure 13). The change in the direction of the major axis of the ellipse is also captured by WRF simulations; the major axis rotates as a function of time during the event in the clockwise sense. The estimated angle of the major axis is $-45°$, $68°$ and $37°$ for 30 October, 31 October and 1 November respectively. This fact also suggests that the changes in the wavenumber vector and wave characteristics may be due to temporal changes in the surface wind direction and magnitude.

3.3. *Propagation: ray back-tracing*

Waves observed with the radiosondes over Ushuaia are concentrated above 12 km height (Figure 3). As the waves are generated by orography, we expect they are fully dispersed and propagating freely at those heights. Therefore, a ray back-tracing technique can be a useful tool to determine the location of the mountains that generated these waves. As previously mentioned, these waves could have been forced by the orography of Tierra del Fuego, but also they could have been generated at the continent and then propagated southeast. Ray-tracing techniques can thus add a further independent evidence apart from WRF simulations on the location and characteristics of the source.

A standard ray-tracing technique (Lighthill, 1978) is applied. The details of the technique are given in Appendix B. The initial position of the wave train and zonal and meridional wavenumber are needed to launch the waves in the ray-tracing technique. The vertical wavenumber is considered as a dependent parameter that is determined from the dispersion relation, assuming the ground-based frequency is zero. The initial position is at Ushuaia (54.7°S, 68.1°W), at a height of 16 km and 24 km, since in this height range waves are found over Ushuaia in the radiosondes and in the WRF simulations. The rest of the unknown variables, namely zonal and meridional wavenumber, have to be determined from the observed wave event.

A wavelet analysis, using a c-Morlet basis, was applied to WRF data to determine the horizontal wavenumber vector around Ushuaia. The zonal wavenumber is estimated using the one-dimensional wavelet transform at 54.7°S and 16 km height. The left panels of Figure 14 show the zonal wavelength as a function of longitude for zonal and meridional wind and potential temperature profiles; a very coherent structure is found in the three variables which peaks at about 370 km wavelength. The meridional wavelength (right panels of Figure 14) is not so clearly detected; the peak appears to be at wavelengths longer than 450 km but regrettably the wavelength is too long to be fully captured by the wavelet analysis. We also attempted to infer the wavenumber directly from the plots. From Figure 9(c) a zonal wavelength of 370 km and a meridional wavelength of 550 km are found. The angle of the horizontal wavenumber vector can also be inferred by inspection from the major axis of the ellipse. From Figure 4 we estimate an angle of about $34 \pm 3°$.

Given the uncertainty in the meridional wavelength, we launched three rays from Ushuaia coordinates at a height of 16 km, having a zonal wavelength (λ_x) of 370 km and meridional wavelengths of $\lambda_y = 500$, 550 and 600 km (the angles of the horizontal wavenumber corresponding to these wavelengths are 36.5, 33.8 and 31.7° respectively). Using these values in the dispersion relation, the resulting vertical wavelength is in the range of 5–6 km which is consistent with the values found in the vertical profiles. The rays propagate back freely down to a height of 2 km at which the ray-tracing is stopped. The rays go nicely back to the continent (see Figure 15) where the highest mountains are located in about 8 hours. The trajectories are influenced by the background conditions; in particular the lateral background shear wind refracts the waves. These changes in the wavenumber in turn produce changes in the trajectory.

A similar procedure was conducted at a height of 24 km. The wavelet analysis (not shown) gives a zonal

Copyright © 2012 Royal Meteorological Society

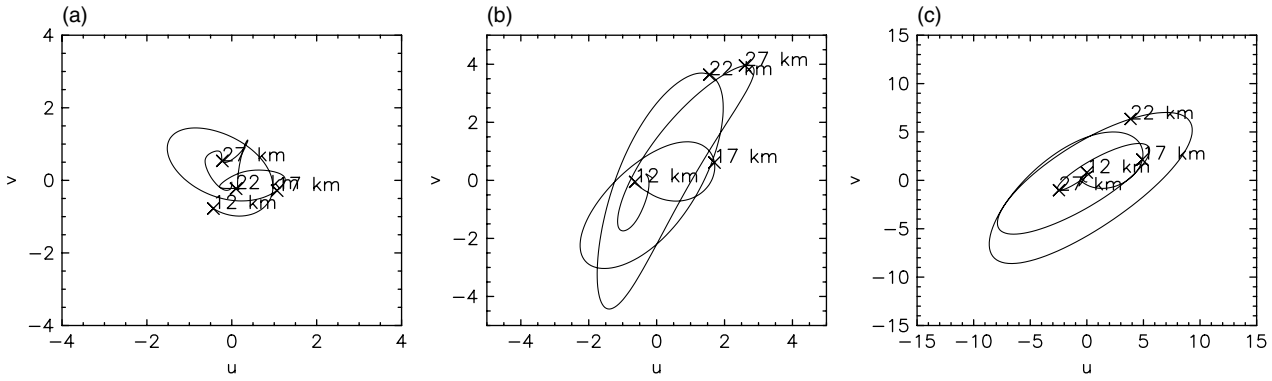

Figure 13. Hodograph for the wind perturbation from the WRF simulation above Ushuaia on (a) 30 October at 1200 UTC, (b) 1 November at 0000 UTC and (c) 1 November at 1200 UTC. Perturbations are obtained with a filtering window of 1–10 km. Points corresponding to a height of 12, 17, 23 and 27 km are shown with a cross.

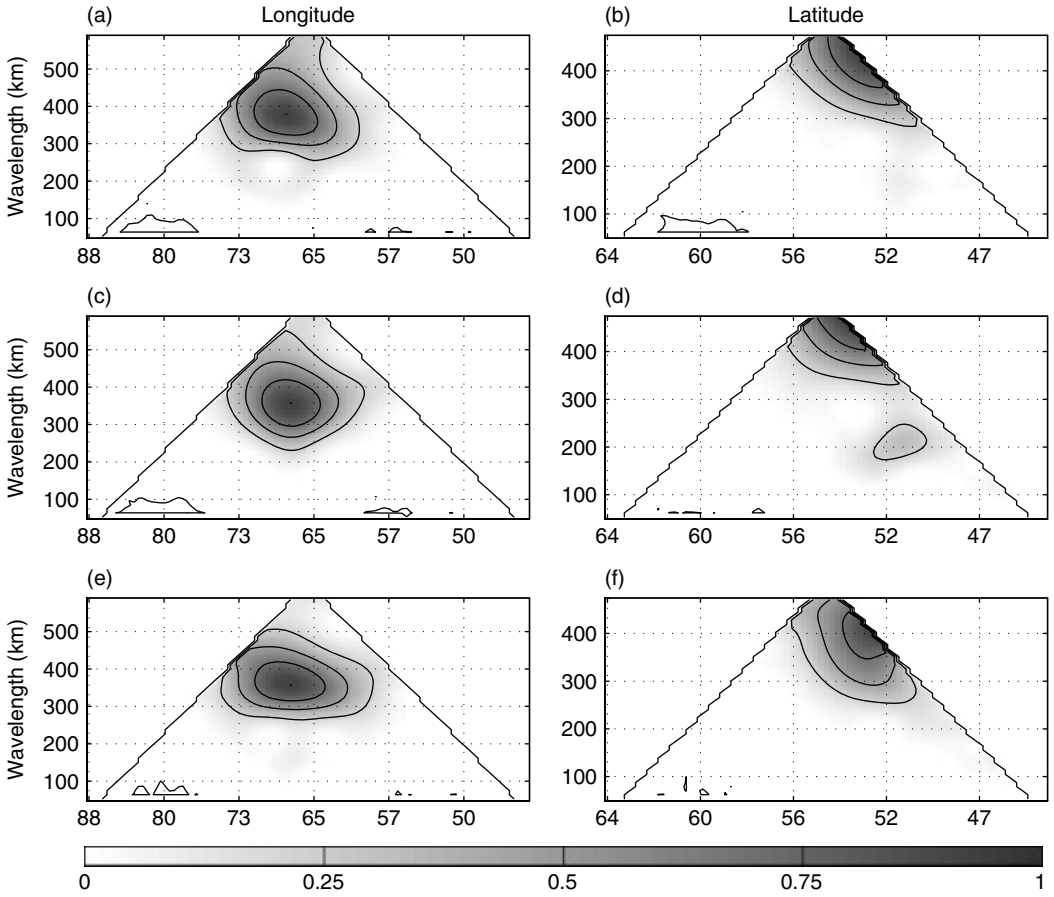

Figure 14. 1D horizontal normalized space-scale energy density at Ushuaia at a height of 16 km on 1 November at 1200 UTC for u (upper panels), v (middle panels) and θ (lower panels) at 54.7°S (left panel) and 68.1°W (right panel).

wavelength of 250 km and a meridional wavelength of about 310 km. As the horizontal wavelengths are shorter, the main horizontal wavelengths of the disturbance over Ushuaia can be determined more accurately. The horizontal wavelengths are in agreement with the one obtained from the radiosondes with the wave analysis in (1). Three rays are launched backwards with $\lambda_x = 270$ km and $\lambda_y = 270$, 300 and 330 km. From 24 km of height, the rays of the disturbance also go back to the continent and are located near the highest mountain when they are at a height of 2 km (Figure 16), showing again that these mountains generate the disturbance. The time that the three rays take to go back from 24 km to 2 km is about 10 h. The trajectories as a function of height (Figure 16(b) and (c)) present slower vertical group speed around 24 km, showing that the waves are closer to their critical levels (in which the vertical group velocity goes to zero).

The effect of wind shear in the lateral propagation of the waves is examined by means of a comparison of the ray path of a wave propagating in real background conditions compared with the ray path of a wave that propagates in uniform background conditions, which are the horizontal averages of the real background conditions. Since the background wind and temperature are horizontally uniform in the last case, the horizontal wavenumber vector is constant. Figure 17 shows the ray paths for the two cases for a wave with horizontal wavelength 370 km and

Copyright © 2012 Royal Meteorological Society

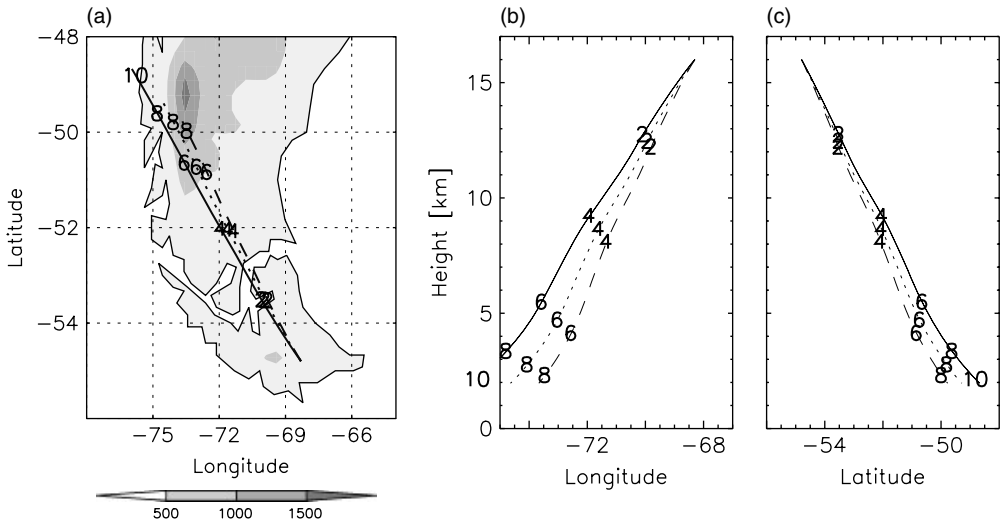

Figure 15. Ray backtracing of the wave train launched at 16 km over Ushuaia, for the waves with $\lambda_x, \lambda_y = 370,\ 500$ km (continuous line), 370, 550 km (dotted line) and 370, 600 km (dashed line) on (a) *x*–*y*, (b) *x*–*z* and (c) *y*–*z* planes. The orography that exceeds 1000 m is shaded. The time of propagation [h] since launch is shown.

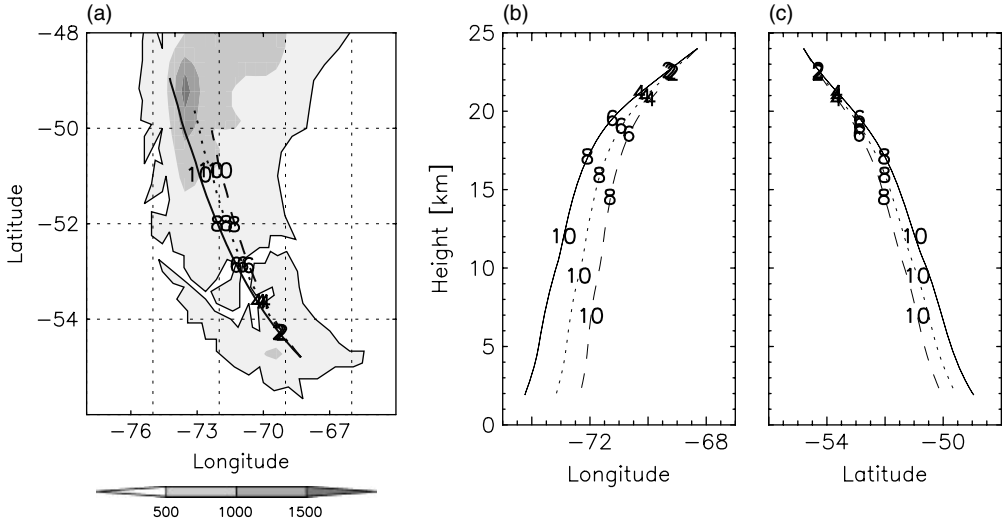

Figure 16. Ray backtracing of the wave train launched at 24 km over Ushuaia for the waves with $\lambda_x, \lambda_y = 270,\ 270$ km (continuous line), 270, 300 km (dotted line) and 270, 330 km (dashed line) on (a) *x*–*y*, (b) *x*–*z* and (c) *y*–*z* plane.

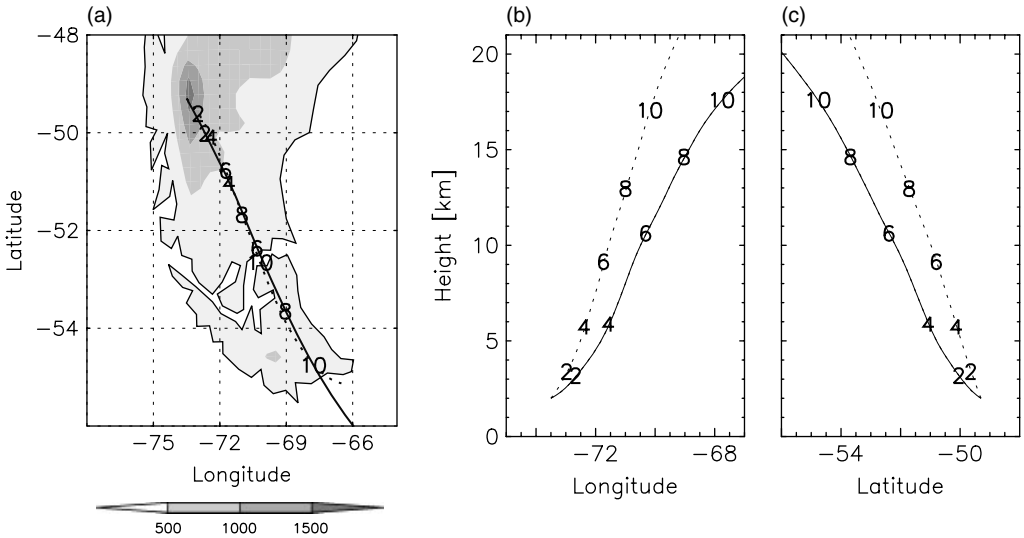

Figure 17. Ray path of the wave train launched over the highest mountain in the continent for control background conditions (continuous line) and horizontally averaged background conditions (dashed line) on the (a) *x*–*y*, (b) *x*–*z* and (c) *y*–*z* planes.

Copyright © 2012 Royal Meteorological Society

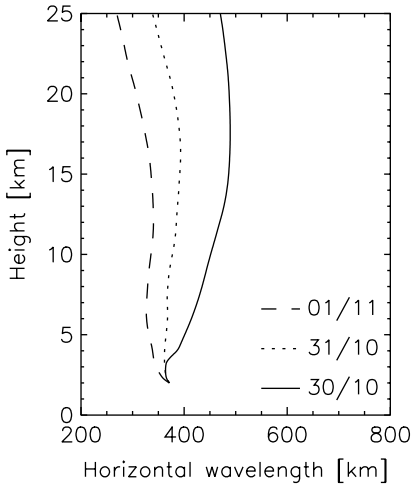

Figure 18. Vertical profile of the horizontal wavelength given by the ray-tracing technique as the waves propagate upward in a horizontal background wind on 30 October at 1200 UTC (continuous line), 31 October at 1200 UTC (dotted line) and 1 November at 1200 UTC (dashed line).

azimuthal angle 24°, which is launched at the location of the highest mountain over the domain. As has been shown, this is the most likely mountain that forced the event. The rays are found to have the same horizontal path in both cases (Figure 17(a)). However, the horizontal propagation is highly enhanced due to the presence of horizontal wind shear. This is clearly seen in Figure 17(b) and (c).

The temporal changes in the horizontal wavelength found at 16 km (see Figure 9) may be produced by changes in the refraction by different horizontal background winds. To evaluate this possibility, we conducted three ray-tracing experiments in which we launched from 2 km height above the highest mountain in the domain ($-73.5°W$, $-49.3°S$) the same initial wave (370 km of horizontal wavelength and an azimuthal angle of 24°) and the wave propagates in the background conditions found on 30 October at 1200 UTC, 31 October at 1200 UTC and 1 November at 1200 UTC (i.e. the background conditions are fixed for each experiment). As time progresses, the horizontal wavelength for each given height is shorter (Figure 18). The resulting horizontal wavelength at 16 km on 30 October at 1200 UTC, 31 October at 1200 UTC and 1 November at 1200 UTC from the ray-tracing analysis is 502.7, 383.0, and 333.4 km respectively. Therefore, the temporal changes in the horizontal background conditions cannot explain the temporal changes found in the horizontal wavelength (see Figure 9).

3.4. Gravity-wave breaking

The measurements performed by the radiosonde launched on 1 November suggest the existence of dynamical instabilities induced by the wave perturbations, and therefore the wave must be breaking (see Figure 5). Furthermore, the ray path presented in Figure 16 shows that the waves propagate toward their critical levels, which are located at a height of 25 km and above. The possible existence in the WRF simulations of convective and dynamical instabilities and wave filtering by critical levels is therefore examined.

Figure 19 shows a x–z cross-section of the potential temperature as simulated by WRF located at 54.7°S on 1 November 1200 UTC (note that the radiosonde was launched at 1144 UTC): the wave induces strong perturbations in the potential temperature field and produces the classical picture of wave overturning, with an important potential temperature discontinuity at about 19 km and 21 km. Above 25 km, the disturbance is strongly damped. Perturbations are not visible above 27 km, suggesting that the disturbance has a critical level around that height and it is unable to reach altitudes higher than the critical level. This feature is independent of the sponge layer; it remains in a simulation with a 5 km deep sponge layer. Indeed, the sponge layer appears to play no role in the simulation due to the presence of the critical level. The wave-induced perturbations in the temperature potential produce a convective instability in the flow at a longitude of 65°. Over Ushuaia, there is a dynamical instability (Figure 19(b)) at 19.3 km where $Ri = 0.08$ and there is no convective instability (Figure 19(c)). The radiosonde measurements over Ushuaia also show dynamical instabilities, but at 13, 18 and 22.2 km (Figure 5). In general, we speculate that there exists a layer between 16 and 24 km where the wavefield contains amplitudes close to the dynamical instability threshold. The unstable layer appears to be narrower in the WRF simulation (see Figures 19(b) and 12(b)).

The zero zonal wind surface, which could be a coarse indicator of critical level,[‡] depends on latitude. The height of the zero zonal wind is 24 km at 50°S and 30 km at 54°S and descends with time. Consequently, we also expect that the overturning height depends on latitude.

4. Conclusions

A spectacular mountain-wave event that occurred over Patagonia was captured by radiosonde measurements and has been further examined using high-resolution WRF simulations. The high-resolution vertical measurements obtained with the radiosondes and combination of these with WRF simulations permitted us to obtain the wave-breaking characteristics in the region. In the wave analysis, the application of some novel techniques gives a clear picture of the synoptic situation during the wave generation, the propagation of the rays and the breaking of the waves.

We have shown that the high wave-activity event observed over Ushuaia on 1 November 1995 is generated by the passage of an extratropical cyclone, which reaches the Chilean coast and then the generated waves propagate southeastward. As the cyclone reaches the continent, it interacts strongly with the mountain range; the cyclone elliptical shape is deformed and its trajectory shows a clear removable discontinuity. The time of the discontinuity in the velocity is identified as the starting time of the wave-triggering event. Further characteristics of the wave event, like duration, amplitude, direction, are linked to the cyclone movement. In the Southern Pacific east of the Andes an important storm track is located, which is well-known for its high-density and high-intensity cyclone activity (Taaljard, 1967; Hoskins and Hodges, 2005), so that we may expect the active periods of wave forcing in the region to be related

[‡]Note that a critical level is produced at the height where the horizontal wavenumber vector is perpendicular to the horizontal background wind, so that the surface in which the zonal wind becomes zero is an indicator of critical levels only for waves that propagate mainly in the zonal direction.

Copyright © 2012 Royal Meteorological Society

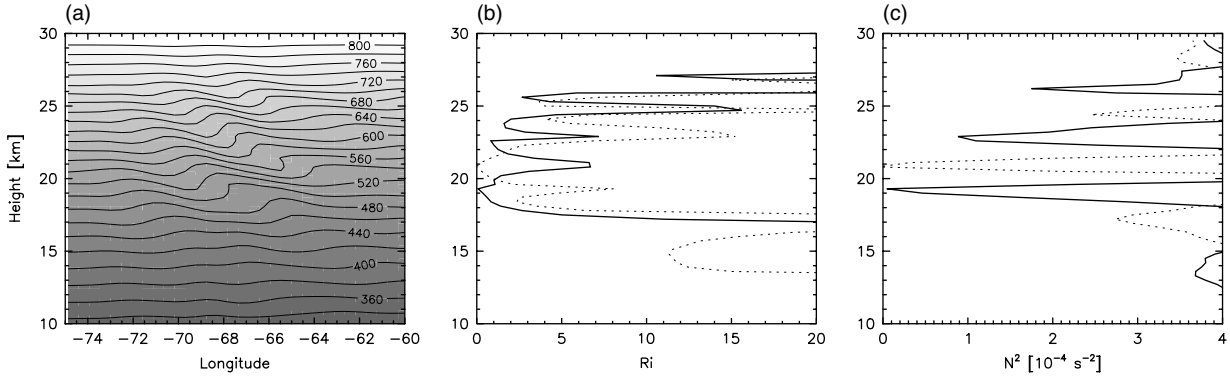

Figure 19. (a) Potential temperature from the WRF simulation at a latitude of 54.7° on 1 November at 1200 UTC. (b) Richardson number at a longitude of 68° (over Ushuaia, continuous line) and 65° (dashed line). (c) The square of the Brunt–Väisälä frequency ($[N^2] = 10^{-4}\,s^{-2}$).

to cyclone activity. Thus, this work raises a hypothesis regarding the high gravity-wave activity found in South America: it may be caused by extratropical cyclones reaching the Chilean coast and soon after finding the Andes mountain range (since the mountains are very close to the coast, the cyclone strength is not reduced much by surface friction). Future work will investigate statistically the relationship of extratropical cyclones in the Pacific ocean and gravity-wave energy in Patagonia region using the automatic tracking of cyclones. In this sense, the present work represents an exhaustive evaluation of the automatic tracking technique for a paradigmatic case study. The combination of the cyclone-tracking technique with a Kalman filter may be devised as an alternative way to forecast the triggering of orographic waves.

The examined wave-forcing event lasts 3 days. Important day-to-day changes in the horizontal wavelength are found. The differences in the refraction from a changing environment were investigated as one possible explanation for these horizontal wavelength changes. The waves were traced with a ray-path technique for every single day of the event: the horizontal wavelength obtained by refraction cannot explain the wavelengths found in the WRF simulation. The wave characteristics change because the surface wind near the mountains that force the disturbance changes its direction during the passage of the cyclone. On 31 October the surface wind is easterly, which appears to generate long waves forced by the Patagonian plateau. Since the cyclone is moving parallel to the coast, this means it is moving in the southward direction; the actual mountains that force the event may also change slightly as a function of time. Furthermore, the time dependence of the magnitude of the surface wind may also play a role (Chen *et al.*, 2005).

Above 20 km of height, waves are found over the sea, southeast of Tierra del Fuego. These waves are identified with the orographic wave event; they propagate long horizontal distances from the orographic source. A combined technique is used: horizontal wavelet analysis determines the characteristics of the waves at the heights where they are observed and then the rays are traced back to the sources. The ray-tracing technique shows that the wave event is forced by surface winds over mountains reaching heights of 1700 m located over the South American continent. Orographic waves that propagate long distances downstream have also been found in satellite observations (Wu and Jiang, 2002; Wu *et al.*, 2006; Alexander *et al.*, 2008) and in modelling studies (Shutts and Vosper, 2011). In this work, we emphasize the long lateral propagation of the waves (by lateral we mean perpendicular to the downstream direction), which are found to propagate laterally over 1500 km with amplitudes of about $5\,m\,s^{-1}$ at those distances. This long lateral propagation is essential to show that orographic waves from the continent propagate towards the Drake Passage. Two effects produce the lateral propagation. One is the lateral background wind shear, as is shown through a ray-tracing analysis. The other is the three-dimensional structure of the shorter waves found in the WRF simulation. They appear to belong to one of the branches of the characteristic V-shaped downstream ship-wave pattern of isolated mountains (Smith, 1980).

There is a strong asymmetry between the north and south branch of the V-shaped pattern of the disturbance; waves are mainly found in the south branch. This asymmetric pattern is not found in simulations with a horizontally uniform background wind in the region (Pulido and Rodas, 2011). One explanation for this asymmetry is the non-uniformity in latitude of the background wind; in particular the height of the critical level changes with the latitude. Waves in latitudes equatorward of −52°S are strongly obliterated by critical-level filtering.

The detection of waves that at first sight look to be inertio-gravity waves because of their elliptical polarization has generated some controversy in previous studies (Cornish and Larsen, 1989; Hines, 1989). In the cases that we examined here, the polarization found for the quasi-stationary mountain waves is elliptical in the stratosphere. This is found in the hodographs derived from the radiosonde measurements and also in the hodographs derived from WRF simulations. Two effects are likely contributing to produce this elliptical polarization: rotation effects and strong shear winds perpendicular to the horizontal wavenumber vector (Hines, 1989). These two effects both induce a perturbation in the direction perpendicular to the horizontal wavenumber vector, the impact of the last effect being much smaller. Moldovan *et al.* (2002) examined an orographic gravity wave that propagates toward its critical level in a rotating atmosphere; they show that the polarization becomes circular toward the inertia critical level. With the help of WRF simulations, we were able to obtain the evolution of the wave perturbation; it is evident that the observed main disturbance is quasi-stationary and its pattern is completely correlated to the Andes mountain range (there are some traces of non-stationary waves which are likely produced by the time-dependent surface winds (Lott and Teitelbaum, 1993), however these waves are smaller 'amplitude and do not contribute to the main

Copyright © 2012 Royal Meteorological Society

disturbance). In agreement with Moldovan *et al.* (2002), a conclusion that we would like to highlight for future observational studies is that rotation effects must be taken into account when considering orographic gravity waves with an intrinsic frequency, $\mathbf{k} \cdot \mathbf{U}$, of the order of f, in other words when the waves are propagating toward the inertia critical levels.

The Richardson number profile obtained from the radiosonde measurements on 1 November (Figure 5) shows a unique behaviour, with several patches from the surface up to 28 km where the Richardson number is below the critical value. To our knowledge, this spectacular wave-breaking behaviour of 28 km vertical depth has not been documented previously. The 1 November radiosonde shows that the wave field is dynamically unstable but no convective instabilities are found in the stratosphere, so that the instability is induced by high wind shear values. The dynamical instability is related to the inertial characteristics found in waves that show elliptical polarization. Inertio-gravity waves are expected to produce dynamical instabilities (Fritts and Yuan, 1989). (The WRF simulations do not appear to simulate the breaking mechanism properly; the unstable layer is narrower with only one unstable peak, also note that convective unstable layers are found in the stratosphere in the WRF simulations.) The Richardson number plot obtained from radiosonde measurements on 1 November (Figure 5) reminds us of the picture as regards simple saturation of the wave field (Lindzen, 1981). The flow reaches the Richardson number threshold due to the large wave amplitude. As the wave amplitude exceeds the threshold, a saturation mechanism is activated, e.g. turbulence is generated, until the wave amplitude attains the threshold value, resulting in a Richardson number profile with several patches very close to the threshold (i.e. $Ri \approx 0.25$, although note that Achatz (2007) found that turbulence can be produced by gravity waves in a flow with Ri values over 0.25). The breaking of these high-amplitude waves produces momentum flux divergences that persist for a period of three days at least, and therefore may produce large influences on the general circulation. In this case study, the observed waves force the lower stratosphere circulation through momentum flux divergences. However, when the Antarctic vortex edge is located over these latitudes, the generated waves in the region are expected to propagate up to the mesosphere, forcing the general circulation there.

The ERA interim reanalyses do not capture the event; there are some signs of mountain forcing in the flow aloft the Andes mountain range, however the mountain-wave event found in the radiosondes and the WRF simulations is not present in ERA interim data. Note that ERA interim data are of 1.5° resolution, which is close to half of the characteristic wavelength of the event (about 280 km). Current ECMWF operational analyses have much higher resolution and therefore are likely to capture those wave events with long wavelengths (e.g. Alexander and Teitelbaum, 2007). Indeed, a simulation performed with the ECMWF forecasting system at $T1279$ and with 91 vertical levels for the examined period (generously provided by an anonymous reviewer) does capture the wave event, and the simulation also confirms the southeastwards propagation of the waves found with the WRF simulations. The WRF simulations in this work show an excellent agreement with the radiosonde data; the amplitude of the waves found in WRF simulations over Ushuaia are very close to those found in the radiosondes. Other general characteristics of the wave field such as vertical wavelength and polarization are also very similar between them, with the exception of the wave-breaking mechanism.

Acknowledgements

We thank the three anonymous reviewers for comments that helped to improve the manuscript. This work was supported by ANPCyT–Argentina under grants PICT 35776 and PICT 2007 No. 411. We thank the European Centre for Medium-Range Weather Forecasts (ECMWF) for providing some of the data used in this work, which were taken from the public ECMWF web site. We also thank the Centre National d'Etudes Spatiales (CNES) for supporting the radiosonde measurements.

Appendix A. Cyclone-tracking algorithm

In order to track cyclones automatically, we developed a simple tracking technique which is mainly based on the work of Blender *et al.* (1997). The algorithm detects for the first frame all the local minima present in the field (e.g. surface pressure or geopotential from ECMWF analysis). The identification of minima is done with a moving window composed of 3×3 grid points; a local minimum is found if the central grid point is strictly smaller than the other points, then a third-order two-dimensional spline (using 5×5 grid points around the grid point identified as the minimum) is fitted so that the location of the minimum of the biquadratic function is identified as the minimum. This methodology improves the resolution of the minimum locations and makes it possible to obtain a smoother cyclone trajectory. The location of the minimum is saved as a probable cyclone seed.

For the subsequent frames, local minima are searched and detected; if any of the new local minima satisfies both a distance criterion with respect to one of the previous frame minima and a smoothness criterion, then this minimum is considered as a new point of the cyclone trajectory. If the new local minimum does not satisfy both criteria, it is identified as a new probable cyclone seed.

A probable cyclone is considered as a cyclone if the track is composed of at least 8 points (8 frames). In other words, the track should last at least 48 hours. This condition removes most of the artificial local minima related to noise in the fields. Furthermore, to remove stationary cyclones and noise extremes generated by the orography (which are stationary and may remain for several frames), the cyclone should propagate at least a distance of 400 km during its whole life cycle.

In this work we use the geopotential field at 1000 hPa from ERA interim (ECMWF). The maximum distance between points of a probable cyclone is set to 400 km (note that each frame is every 6 h). The smoothness/continuity criterion is based on the velocity of the cyclone. The velocity angle of the last point is compared with the mean velocity of the previous four last points; if the angle difference exceeds 90° then the new minimum point is rejected.

Copyright © 2012 Royal Meteorological Society

Appendix B. Ray-tracing technique

Ray-tracing theory is introduced in Lighthill (1978). The ray-tracing equations are

$$\frac{\mathrm{d}x}{\mathrm{d}t} = \frac{\partial \omega}{\partial k}, \tag{B1}$$

$$\frac{\mathrm{d}y}{\mathrm{d}t} = \frac{\partial \omega}{\partial l}, \tag{B2}$$

where x and y are the longitude and latitude over the sphere in the numerical scheme and ω is the absolute frequency. The wavenumber vector is $\mathbf{k} = (k, l, m)$ and its evolution is governed by

$$\frac{\mathrm{d}k}{\mathrm{d}t} = -\frac{\partial \omega}{\partial x}, \tag{B3}$$

$$\frac{\mathrm{d}l}{\mathrm{d}t} = -\frac{\partial \omega}{\partial y}, \tag{B4}$$

$$\frac{\mathrm{d}m}{\mathrm{d}t} = -\frac{\partial \omega}{\partial z}. \tag{B5}$$

The dispersion relationship is equal to the one used in Marks and Eckerman (1995):

$$(\omega - kU - lV)^2 = \frac{N^2(k^2 + l^2) + f^2(m^2 + \alpha^2)}{k^2 + l^2 + m^2 + \alpha^2}, \tag{B6}$$

where N is the Brunt–Väisälä frequency, f the inertial frequency, U and V the components of the background wind and $\alpha = 1/(2H)$, where H is the density scale height.

The dispersion relationship (B6) is used in the ray equations (B1)–(B4).

The ray equations (B1)–(B4) are expressed as finite differences. The given initial conditions are the initial position x, y, z and the initial horizontal wavenumber k, l. The absolute frequency is assumed to be zero. At each time step the vertical wavenumber is calculated from (B6) with $\omega = 0$, so that (B5) is not required. The mean fields are taken from WRF simulations using an averaging moving window of 40 points. These fields are interpolated bilinearly to the ray position. The derivative of N and α as a function of x and y in (B3) and (B4) are considered negligible (we did some preliminary-order calculations in which these terms were found to be negligible for the range of waves that we examined in this work). Wind-shear terms in (B3) and (B4) are considered and have an important effect.

In order to produce the back-tracing ray analysis a negative time step is used.

References

Achatz U. 2007. Gravity-wave breaking: Linear and primary nonlinear dynamics. *Adv. Space Res.* **40**: 719–733.

Alexander MJ, Teitelbaum H. 2007. Observation and analysis of a large amplitude mountain wave event over the Antarctic peninsula. *J. Geophys. Res.* **112**: D21103.

Alexander MJ, Gille J, Cavanaugh C, Coffey M, Craig C, Eden T, Francis G, Halvorson C, Hannigan J, Khosravi R, Kinnison D, Lee H, Massie S, Nardi B, Barnett J, Hepplewhite C, Lambert A, Dean V. 2008. Global estimates of gravity wave momentum flux from High Resolution Dynamics Limb Sounder observations. *J. Geophys. Res.* **113**: D15S18. DOI:10.1029/2007JD008807.

Alexander MJ, Geller M, McLandress C, Polavarapu S, Preusse P, Sassi F, Sato K, Eckermann S, Ern M, Hertzog A, Kawatani Y, Pulido M, Shaw T, Sigmond M, Vincent R, Watanabe S. 2010. Recent developments in gravity wave effects in climate models, and the global distribution of gravity wave momentum flux from observations and models. *Q. J. R. Meteorol. Soc.* **136**: 1103–1124.

Alexander SP, Klekociuk AR, Tsuda T. 2009. Gravity wave and orographic wave activity observed around the Antarctic and Arctic stratospheric vortices by the COSMIC GPS-RO satellite constellation. *J. Geophys. Res.* **114**: D17103. DOI:10.1029/2009JD011851.

Blender R, Fraedrich K, Lunkeit F. 1997. Identification of cyclone track regimes in North Atlantic. *Q. J. R. Meteorol. Soc.* **123**: 727–741.

Chen C-C, Durran DR, Hakim GJ. 2005. Mountain-wave momentum flux in an evolving synoptic-scale flow. *J. Atmos. Sci.* **62**: 3213–3231, DOI:10.1175/JAS3543.1.

Chun H-Y, Goh J-S, Kim Y-H. 2007. Characteristics of inertio-gravity waves revealed in rawinsonde data observed in Korea during 20 August to 5 September 2002. *J. Geophys. Res.* **112**: D16108. DOI:10.1029/2006JD008348.

Cornish CR, Larsen MF. 1989. Observations of low-frequency inertia–gravity waves in the lower stratosphere over Arecibo. *J. Atmos. Sci.* **46**: 2428–2439.

Eckermann SD, Preusse P. 1999. Global measurements of stratospheric mountain waves from space. *Science* **286**: 1534–1537.

Ern M, Preusse P, Alexander MJ, Warner CD. 2004. Absolute values of gravity wave momentum flux derived from satellite data. *J. Geophys. Res.* **109**: D20103. DOI:10.1029/2004JD004752.

Fritts DC, Yuan L. 1989. Stability analysis of inertio–gravity wave structure in the middle atmosphere. *J. Atmos. Sci.* **46**: 1738–1745.

Garcia RR, Boville BA. 1994. Downward control of the mean meridional circulation and temperature distribution of the polar winter stratosphere. *J. Atmos. Sci.* **51**: 2238–2245.

Hines CO. 1989. Tropopausal mountain waves over Arecibo: A case study. *J. Atmos. Sci.* **46**: 476–488.

Holton JR. 1992. *An introduction to dynamic meteorology*. 3rd edn. Academic Press: New York.

Hoskins BJ, Hodges KI. 2005. A new perspective on Southern Hemisphere storm tracks. *J. Climate* **18**: 4108–4129, DOI:10.1175/JCLI3570.1.

Lighthill J. 1978. *Waves in fluids*. Cambridge University Press: Cambridge.

Lindzen RS. 1981. Turbulence and stress owing to gravity wave and tidal breakdown. *J. Geophys. Res.* **86**: 9707–9714.

Lott F, Teitelbaum H. 1993. Topographic waves generated by a transient wind. *J. Atmos. Sci.* **50**: 2607–2624.

Marks C, Eckermann SD. 1995. A three-dimensional nonhydrostatic ray-tracing model for gravity waves: Formulation and preleminary results for the middle atmosphere. *J. Atmos. Sci.* **52**: 1959–1984.

Moldovan H, Lott F, Teitelbaum H. 2002. Wave breaking and critical levels for propagating inertio-gravity waves in the lower stratosphere. *Q. J. R. Meteorol. Soc.* **128**: 713–732.

O'Sullivan D, Dunkerton T. 1995. Generation of inertia–gravity waves in a simulated life cycle of baroclinic instability. *J. Atmos. Sci.* **52**: 3695–3716.

Plougonven R, Hertzog A, Teitelbaum H. 2008. Observations and simulations of a large-amplitude mountain wave breaking over the Antarctic Peninsula. *J. Geophys. Res.* **113**: D16113. DOI:10.1029/2007JD009739.

Pulido M, Thuburn J. 2008. The seasonal cycle of gravity-wave drag in the middle atmosphere. *J. Climate* **21**: 4664–4679. Corrigendum in *J. Climate* **22**: 2572–2572 .

Pulido M, Rodas C. 2011. A higher-order ray approximation applied to orographic gravity waves: Gaussian beam approximation. *J. Atmos. Sci.* **68**: 46–60, DOI:10.1175/2010JAS3468.1.

Scavuzzo C, Lamfri M, Teitelbaum H, Lott F. 1998. A study of the low-frequency inertio-gravity waves observed during PIREX. *J. Geophys. Res.* **103**: 1747–1758.

Shutts GJ. 1998. Stationary gravity-wave structure in flows with directional wind shear. *Q. J. R. Meteorol. Soc.* **124**: 1421–1442.

Shutts GJ, Vosper SB. 2011. Stratospheric gravity waves revealed in NWP model forecasts. *Q. J. R. Meteorol. Soc.* **137**: 303–317.

Simmons A, Uppala S, Dee D, Kobayashi S. 2007. ERAInterim: New ECMWF reanalysis products from 1989 onwards. *ECMWF Newsletter* **110**: 25–35.

Skamarock WC, Klemp JB, Dudhia J, Gill DO, Barker DM, Wang W, Powers JG. 2005. '*A description of the Advanced Research WRF*

Copyright © 2012 Royal Meteorological Society

Version 2', NCAR Technical Note NCAR/TN-468+STR, 88 pp. NCAR: Boulder, Colorado, USA.

Smith RB. 1980. Linear theory of stratified hydrostatic flow past an isolated mountain. *Tellus* **32**: 348–364.

Song I-S, Chun H-Y, Garcia RR, Boville BA. 2007. Momentum flux spectrum of convectively forced internal gravity waves and its application to gravity-wave drag parameterization. Part II: Impacts in a GCM (WACCM). *J. Atmos. Sci.* **64**: 2286–2308.

Taaljard JJ. 1967. Development, distribution and movement of cyclones and anticyclones in the Southern hemisphere during IGY. *J. Appl. Meteorol.* **6**: 973–987.

Trenberth KE. 1991. Storm tracks in the Southern Hemisphere. *J. Atmos. Sci.* **48**: 2159–2178.

Uccellini L, Koch S. 1987. The synoptic setting and possible energy sources for mesoscale wave disturbances. *Mon. Weather Rev.* **115**: 721–729.

Vincent RA, MacKinnon A, Reid IM, Alexander MJ. 2004. VHF profiler observations of winds and waves in the troposphere during the Darwin Area Wave Experiment (DAWEX). *J. Geophys. Res.* **109**: D20S02. DOI:10.1029/2004JD004714.

Wu DL, Eckermann SD. 2008. Global gravity wave variances from Aura MLS: Characteristics and interpretation. *J. Atmos. Sci.* **65**: 3695–3718.

Wu DL, Jiang JH. 2002. MLS observations of atmospheric gravity waves over Antarctica. *J. Geophys. Res.* **107**: 4773, DOI:10.1029/2002JD002390.

Wu DL, Preusse P, Eckermann SD, Jiang JH, de la Torre Juarez M, Coy L, Wang DY. 2006. Remote sounding of atmospheric gravity waves with satellite limb and nadir techniques. *Adv. Space Res.* **37**: 2269–2277.

Copyright © 2012 Royal Meteorological Society